Facile synthesis of solar active charcoal passivated Ag_3PO_4 and their two-channel mechanisms for H_2O_2 formation in aerated water

Owolabi M. Bankole[1*], Olayinka S. Adanlawo[1], Kehinde I. Ojubola[1], Faith O. Adeyemi[1], Ojodomo J. Achadu[2,3], Joseph A. Ogunniyi[1], Segun E. Olaseni [1], Adeniyi S. Ogunlaja[4]

[1]*Hydrochemistry Research Laboratory, Adekunle Ajasin University, Akungba, Nigeria.*
[2]*Chemistry Department, University of Warwick, Coventry, CV4 7AL, United Kingdom.*
[3]*Institutue of Advanced Study, University of Warwick, Coventry, CV4 7AL, United Kingdom.*
[4]*Department of Chemistry, Nelson Mandela University, Port Elizabeth, South Africa.*

Abstract

This work presents the use of activated charcoal passivated-Ag_3PO_4 (CAgP) and bare Ag_3PO_4(AgP) nanoparticles (NPs) as effective photocatalysts for the generation of hydrogen peroxide (H_2O_2) in air-saturated water containing either formic acid (FA) or silver nitrate ($AgNO_3$). The synthesized CAgP and pristine AgP were characterized using various state-of-the-art optical and electron microscopy techniques. The CAgP composites showed remarkable photocatalyzed H_2O_2 formation compared to bare AgP NPs. The CAgP photocatalyzed-assisted H_2O_2 formation from O_2-saturated water under sunlight was achieved via two-channel mechanisms. First, in the presence of FA as a hole scavenger, enhanced H_2O_2 formation was facilitated by decomposition of FA to produce proton (H^+), followed by a spontaneous reduction of dissolved molecular oxygen by the photo-excited electrons. The second photocatalytic pathway involves the formation of H_2O_2 in the absence of electrons (using $AgNO_3$ as an electron scavenger) which occurred via oxidation of H_2O by photo-induced holes to generate hydroxyl radicals ($^{\bullet}HO$) and the combination of photogenerated $^{\bullet}HO$ to produce H_2O_2. The most notable feature of CAgP composite as a photocatalyst is the ease of H_2O_2 formation in O_2/H_2O and O_2/H_2O/FA system, as well as the ability to reuse the recovered CAgP catalyst for a few reaction cycles without losing substantial catalytic activity or mass.

Keywords: Ag_3PO_4 nanoparticles; hydrogen peroxide formation; hole scavengers; photocatalysis; electron scavengers;charcoal passivated Ag_3PO_4.

*Corresponding author. Tel: + 2348034018955; E-mail: bankolemutolib@yahoo.com.

Electronic copy available at: https://ssrn.com/abstract=4091672

Introduction

Hydrogen peroxide (H_2O_2) is a colourless liquid that easily mixes with water or other organic solvents to produce non-toxic reagents [1]. Because of its nontoxicity and greener nature, H_2O_2 is a superior energy transporter or storage system than H_2 and may be safely moved from one location to another [2,3]. For many decades after its discovery and isolation in 1818 by Louis Jacques Thenard [4], H_2O_2 has consistently played a central role as a versatile oxidant in a variety of applications, including deodoriser for wastewater purification, disinfectant or antiseptic for wounds dressing and mouthwash, organic chemical synthesis and transformation, and as a bleaching agent in the textile and paper industries [5]. H_2O_2 spontaneously decomposes into water and oxygen ($2H_2O_2 \rightarrow 2H_2O + O_2$) as the two major products when exposed to ultraviolet (UV) or visible light, thus adding to the safety of its use in industry and at home [2,3]. To increase small-scale synthesis and satisfy expanding demand, researchers are exploring other cost-effective and sustainable methods of producing H_2O_2 utilizing low-cost catalytic materials [2].

The current large-scale industrial production of H_2O_2 relies on a BASF-developed anthraquinone auto-oxidation (AO) technology, in which alkylanthraquinone (AAQ) sequentially undergo series of hydrogenation reactions in the presence of palladium catalysts to form dihydroanthraquinone (DAQ) ($AAQ + H_2 \overset{\text{Pd Cat}}{\Rightarrow} DAQ$), followed by oxygenation of the resultant DAQ to yield H_2O_2 and AAQ ($DAQ + O_2 \rightarrow H_2O_2 + AAQ$) [2,5]. The AO technique requires large energy consumption for the hydrogenation and oxidation stepwise reactions and therefore not cost-effective or practicable for small-scale H_2O_2 synthesis [2]. The direct mixing of H_2 and O_2 gases on the other hands, which has been proposed as an alternative approach to anthraquinone oxidation method for H_2O_2 production over noble metal catalysts, is also regarded to be environmentally unsafe due to the possibility of explosions from the mixing of H_2 and O_2 gases [6,7]. As a result of the evaluations of the available technologies, the advanced oxidation process (AOP) driven by UV or visible light radiation in the presence of a suitable photocatalyst is a sustainable and cost-effective option for producing H_2O_2 using water and atmospheric oxygen as the only primary ingredients [8].

Photocatalytic advanced oxidation processes utilizing visible-light-driven catalytic materials, including TiO_2, g-C_3N_4, Ag_2O_3, AgX (X, Cl, Br, I), and other silver-based photocatalysts, have been reported by different research groups to produce significant amounts of H_2O_2 from aerated water in the presence of hole and electron scavengers [2,9-11]. Silver-based photocatalysts, in

Electronic copy available at: https://ssrn.com/abstract=4091672

particular, have demonstrated outstanding photocatalytic performance to thermodynamically drive the formation of H_2O_2 due to their conduction band edges being more negative($< 0.6\ eV\ vs.\ NHE, pH\ 7$) than the redox potential of O_2/H_2O_2 at 0.68 eVvs. NHE, and their valence band edges being lower (more positive) than the redox potentials of $OH^-/^{\bullet}OH$ and O_2/H_2O at $+1.99$ and $+1.23$ eV (vs. NHE, pH 7), respectively [10,11]. The remarkable photocatalytic performances of silver-based photocatalysts are however tainted by their uncontrollable decomposition and photo-corrosion caused by the interaction of surface plasmon resonance of Ag^+ with photo-excited electrons, which transforms Ag^+ into black metallic Ag^0 particles when exposed to UV or visible photons for long periods of time [12,13]. Yang and coworkers [14] reported that using graphene (GR) and graphene oxides (GO) as stable coverage of Ag_3PO_4 effectively shielded the Ag_3PO_4 from photo-decomposition and restrained the recombination of photo-induced electron with holes during photocatalysis, resulting in improved photostability and performance of Ag_3PO_4-graphene composites over bare Ag_3PO_4. The bare Ag_3PO_4 catalyst which is proposed in the current work has high tendency to decompose into Ag^0 and PO_4^{3-} ($Ag_3PO_4 + 3e^- \rightarrow 3Ag^0 + PO_4^{3-}$) when irradiated in the absence of photo-thermally stable solid supports such as carbon-based nanostructures [14]. Thus, activated charcoal is proposed here as a solid support to passivate Ag_3PO_4 in order to fabricate activated carbon-Ag_3PO_4 (CAgP) composite with overall improved stability, catalytic activity, and performance for photocatalyzed H_2O_2 production.

Herein, raw coconut hardwood charcoal was first acidified in 0.1 M HCl to remove alkaline and alkaline-earth metals from its surface and endow it with various oxygen functional groups that provided active sorption sites for Ag^+ (aq. $AgNO_3$) *via* electrostatically driven interaction, followed by the precipitation of Ag_3PO_4 using disodium hydrogen phosphate (Na_2HPO_4). Pal *et al.* [11] fabricated magnetically recyclable photocatalysts for H_2O_2 formation using starch functionalized Fe_3O_4@Ag@Ag_2O nanocomposites. They demonstrated that the best photocatalyst (C1), with VB and CB edges at 2.63 and 0.4 eV, respectively, thermodynamically facilitated water oxidation and $2e^-$ reduction of molecular oxygen to produce H_2O_2 [11]. Interestingly, the photo-induced holes in AgP/CAgP have a better thermodynamic driving force than C1 to generate $^{\bullet}OH$ radicals and water oxidation to produce H_2O_2, because the potentials of the top of VB of AgP/CAgP are more positive at 2.79-2.84 eV than the VB edge of C1. Similarly, the edges of CB of AgP/CAgP are more negative than 0.68 eV, indicating that photocatalytic formation of H_2O_2 in O_2-saturated water is a high possibility. Thus, through $2e^-$ reduction of O_2 and water oxidation,

Electronic copy available at: https://ssrn.com/abstract=4091672

both AgP and CAgP satisfy two-channel pathways for H_2O_2 formation. When the reaction is carried out in the presence of hole scavengers such as organic acids and alcohols, photo-excited electrons at the CB constitute the main driving factor for the production of H_2O_2 [11,15]. Photo-induced holes also drive the formation of H_2O_2 at the VB when an electron scavenger such as silver nitrate is added to the O_2-water system [10,15]. Premised on the above, the photocatalytic performances of bare AgP and CAgP for the generation of H_2O_2 in the presence of hole and electron scavengers were tested. Also, the two-channel plausible mechanisms for the formation of H_2O_2 in water at VB and CB were elucidated.

2.0. MATERIALS AND METHODS

2.1 Material

Silver nitrate ($AgNO_3$, $> 99.7\%$), Potassium titanium oxalate dihydrate (PTO, $K_2[TiO(C_2O_4)_2].2H_2O$, formic acid (FA, 85%), benzoquinone (BQ), isopropyl alcohol (*i*PA) and sodium phosphate dibasic dodecahydrate ($Na_2HPO_4.12H_2O$) were purchased from Sigma Aldrich. Methanol, ethyl alcohol ethanol (%), Commercial H_2O_2(30% v/v) sodium hydroxide (NaOH), hydrochloric acid (HCl) and deionized water was purchased from Pascal Scientific Limited, Nigeria, and were used as received without purification.

2.2 Materials syntheses

2.2.1 Preparation of raw charcoal

The raw coconut hardwood charcoal (200 g) was graciously donated to our laboratory by Prime Coal Plant, Lagos, Nigeria, and the product description as provided by the supplier are listed in Table 1. The charcoal was washed three times with deionized water to remove sands and debris, and then dried in an oven at 60°C for 12 h. Thereafter, it was ground with a mortar and pestle, then pulverized into fine particle sizes using an electric blender (Model: HFB-3489, (China). The pulverized charcoal was then sieved for uniform particle size distribution using a 0.25nm sieve and stored for further use.

Table 1: Supplier description of coconut hardwood charcoal

Electronic copy available at: https://ssrn.com/abstract=4091672

Coconut hardwood charcoal (Wt)	Specifications (%)
Fixed carbon content	86
Ash content	3 (Max. on Dry Basis)
Moisture	5
Volatile matter	3
Burning time	3.5 h
Shape	Irregular lengths (3-28cm)

2.2.2 Preparation of charcoal-supported silver phosphate composite (CAgP)

The powdered particles of the hardwood charcoal were acidified with HCl to remove the oxides of alkaline and alkaline-earth metals present in the charcoal and to enhance its surficial and textural properties prior to immobilization of AgP. Briefly, 1 g of charcoal powder was stirred in 100 mL of HCl (0.1 M) solution at 60^{o}C for 1 h. The treated charcoal was recovered by centrifugation, washed with DI water and dried at 80^{o}C for 24 h. Silver phosphate NPs was adsorbed to the surface of the treated charcoal by precipitation method to prepare charcoal-supported AgP (C/AgP) composites. Typically, 0.1 g of acidified charcoal was sonicated in deionized water (100 mL) for 3 h to give charcoal aqueous dispersions. Then 0.5 g of $AgNO_3$ in deionized water (50 mL) was added drop wise to the charcoal dispersions and the mixture was further sonicated for 3 h to ensure optimal charcoal-Ag^+ adsorption-desorption equilibrium. Under constant stirring, aqueous solution of $Na_2HPO_4.12H_2O$ (1 M, 50 mL) was slowly added into the charcoal-Ag^+ solution at the rate of 5 mL/min for 10 min. The resulting black-yellow precipitate of C/AgP composite was magnetically refluxed for another 5 h at 80 ^{o}C. The product (C/AgP) was washed by centrifuge using deionized water and with absolute EtOH, and dried at 60℃ for 12 h. For comparison, pristine silver phosphate (AgP) NPs were prepared by the same method reported for CAgP composite but without treated charcoal. The synthesized CAgP and AgP were kept in a dark container and stored.

2.3. Materials characterization

Electronic copy available at: https://ssrn.com/abstract=4091672

The solid reflectance spectra of charcoal, AgP and CAgP were recorded on a Shimadzu UV-VIS-NIR Spectrophotometer UV-3100 with a MPCF-3100 sample compartment with samples mounted between two quartz discs which fit into a sample holder coated with barium sulfate. The spectra were recorded over the wavelength range of 800-300 nm, and the scans were conducted at a medium speed using a 20 nm slit width. Fourier transform infra-red (FTIR) spectra were recorded on a Thermo Fisher Scientific FTIR spectrophotometer, using pressed KBr pellets. Transmission electron microscope (TEM) images of the samples were recorded using a JEOL JEM-2010 electron microscope operating at 200 KV. Surface morphologies of AgP and CAgP were analysed using a scanning electron microscope (SEM) equipped with energy dispersive analysis of X-ray equipment (EDAX) (XL 30 FEG ESEM). Raman spectroscopy Raman spectra for the samples were collected using A WITec alpha 300 RAS+ confocal micro-Raman spectrometer (Ulm, Germany) with 532 nm laser wavelength and a spectral acquisition time of 120 s was used to characterize the sample. To minimize the heating effects of the sample, a power of 3.41 mW was applied to the samples. X-ray photoelectron spectroscopy (XPS) analysis of the AFe was performed on a Kratos Axis Ultra X-ray Photoelectron Spectrometer equipped with a monochromatic Al K_α source (1486.6 eV). The hydrodynamic size distributions of AFe NPs, AFeAMX composite and AMX were measured using Malven Dynamic Light Scattering (DLS), Malven, UK. The XRD spectra of the samples were obtained with Bruker D8 ADVANCE diffractometer (Germany) using Cu Kα (1.5406 Å) radiation.

2.4 Photocatalytic formation of hydrogen peroxide (H_2O_2)

Photocatalytic hydrogen peroxide formation over pristine AgP and CAgP photocatalysts were investigated using O_2-saturated deionized water system under natural solar illumination. In a typical representative photocatalytic experiment, 20 mg of AgP or CAgP were dispersed into 50 mL of DI in 250 mL round bottom flask, and the suspension was sonicated for 1 h under dark to ensure complete dispersion of the catalyst in solution and establish adsorption-desorption equilibrium of the reacting mixture. Prior to solar illumination, the reaction mixture was bubbled with O_2 through a syringe needle, and the reaction vessel mounted on a retort stand at a 60° angle and directly irradiated for 5 h by natural sunlight of an average intensity of 615.42 W/m^2. Samples from the reacting mixture were regularly withdrawn at 1 h of solar irradiation, and filtered with syringe filter to separate the catalysts from the filtrates. The concentrations of hydrogen peroxide

Electronic copy available at: https://ssrn.com/abstract=4091672

in the filtrates were determined by colorimetrically using potassium titanium oxalate-sulfuric acid (PTO) reagents [16, 17].

2.4.1. Colorimetric analysis of H_2O_2

The amount of H_2O_2 generated was determined colorimetrically using potassium titanium oxalate method [17]. A stock solution of titanium oxalate reagent containing mixture of $K_2[TiO(C_2O_4)_2].2H_2O$ (0.02 M), and conc. H_2SO_4 (0.5 M) was prepared in 250 mL volumetric flask and used for further studies. The yield of H_2O_2 in the recovered filtrate was determined as follows: 2.5 mL each of the recovered filtrate and the titanium oxalate reagent was pipette into 10-mL flask and make up to the mark with deionized water. Blank solution of titanium reagent (2.5 mL) diluted to 10 mL mark was also prepared without the addition of the filtrate (peroxide). The absorbance of both blank and test samples were measured on the UV-Vis spectrophotometer at wavelength of ca. 400 nm, corresponding to the λ_{max} of titanium (1V)-peroxide complex, **Scheme 1**. The molar concentration of H_2O_2 (in $\mathrm{mol/L}$) was determined by subtracting the absorbance of the blank solution (A_b) from the absorbance of peroxide-containing filtrate (A_p) at wavelength of 400 nm using **Eqn. 1**:

$$[H_2O_2] = \frac{A_p - A_b}{x l \varepsilon_{400}} * V_T \qquad \mathbf{1}$$

where ε_{400} is the molar absorptivity of titanium (IV)-peroxide complex ($9351/\mathrm{mol}^{-1}\mathrm{cm}^{-1}$); A_b and A_p are respectively the absorbance of the blank and peroxide solutions; x is the volume of the peroxide solution (2.5 mL or 25 cm); l is the path length (in cm) of the spectrophotometer cell, and V_T is the total volume of the blank or peroxide solution (10 mL or 100 cm).

2.4.1.1. Standard calibration curve for hydrogen peroxide (H_2O_2) solution

A stock solution of the hydrogen peroxide (H_2O_2) solution was prepared by diluting 1 mL of commercial H_2O_2 (30% v/v) to 2000 mL using double distilled water. Further dilutions were made by adding 5 mL of acidified PTO reagents (0.02 M PTO and 0.05 M H_2SO_4) separately to 0.2, 0.4, 0.6, 0.8 and 1 mL from the standard H_2O_2 solution and diluted them to 10 mL separately in five different labelled conical flasks. The standard calibration curve was plotted between known concentrations (0.2 to 1 mL) of H_2O_2 solutions against their respective absorbance at a wavelength

Electronic copy available at: https://ssrn.com/abstract=4091672

of 400 nm (λ_{max} of PTO-H_2O_2 complex) on UV-Vis spectrophotometer. H_2O_2 concentration formed over the photocatalysts was extrapolated from the plotted standard calibration curve [18].

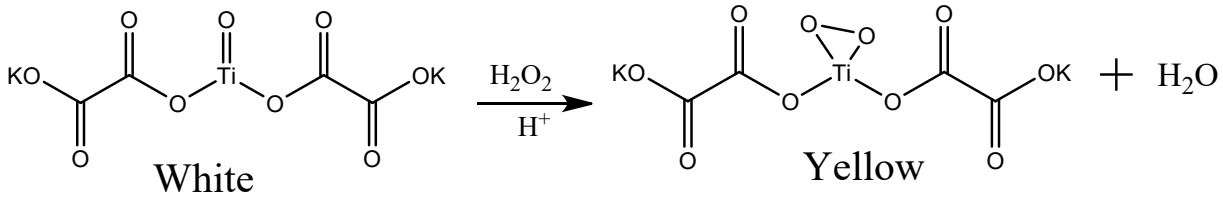

Scheme 1: Reaction between acidified potassium titanium oxide oxalate, PTO, and hydrogen peroxide to give titanium (1V)-peroxide complex.

Blank experiments were also carried out to determine the importance of solar irradiation, photocatalyst(s), and electron donor for hydrogen peroxide formation. The blank experiments were either conducted with only photocatalysts dispersed in O_2-saturated DI water but no electron donor (formic acid), or with formic acid (5%) in solution but no photocatalysts. Experiments in the presence of both photocatalysts and formic acid under dark reaction conditions were also conducted to demonstrate the importance of solar irradiation for the formation of hydrogen peroxide.

2.4.2 *In situ* active species capture experiment

Photocatalytic trapping experiments to investigate the role of active specie and their mechanistic pathways during the formation of hydrogen peroxide over as-synthesized photocatalysts were carried out using silver nitrate ($AgNO_3$), benzoquinone (BQ), and isopropyl alcohol (*i*PA) as radical scavengers to mask the *in-situ* formation of electron, $\bullet O_2^-$, and hydroxyl radical (•OH), respectively. The procedures for the experiments were similar to the method reported for the photocatalytic formation of hydrogen peroxide in the presence of AgP and CAgP, except that 1 mM of scavengers were separately added to the solution and the mixtures were irradiated for 6 h under sunlight.

3. Results and discussions

3.1. Phase structure analysis

Figure 1 displays the phase structures of treated charcoal, pristine AgP and CAgP composite as elucidated using XRD technique. The characteristic X-ray diffraction patterns of treated charcoal

Electronic copy available at: https://ssrn.com/abstract=4091672

at 2θ = 24◦, and 26.78◦ are typical of graphite-type reflections and consistent with the peaks of carbon-based biomass[19, 20], while the distinct diffraction patterns of pristine AgP at 2θ = 20.8°, (110), 29.6°, (200), 33.2°, (210), 36.5°, (211), 42.8°, (220), 47.6°, (310), 52.6°, (222), 54.8°, (320), 57.1°, (321) conform well with the standard diffraction planes of body centred cubic and crystalline Ag_3PO_4 with JCPDS card No. 71-1836 , Figure 1. All the diffraction patterns in pure AgP are conspicuously visible in the diffractogram of the CAgP composites. The crystallinity and intensity of diffraction patterns of AgP in CAgP are however lower than the pure AgP, due to the change in the environment of AgP after composition with charcoal. The absence of diffraction peaks of charcoal in the XRD patterns of CAgP is due to the low weight percentage (wt%) of charcoal used for the preparation of the composite.

Electronic copy available at: https://ssrn.com/abstract=4091672

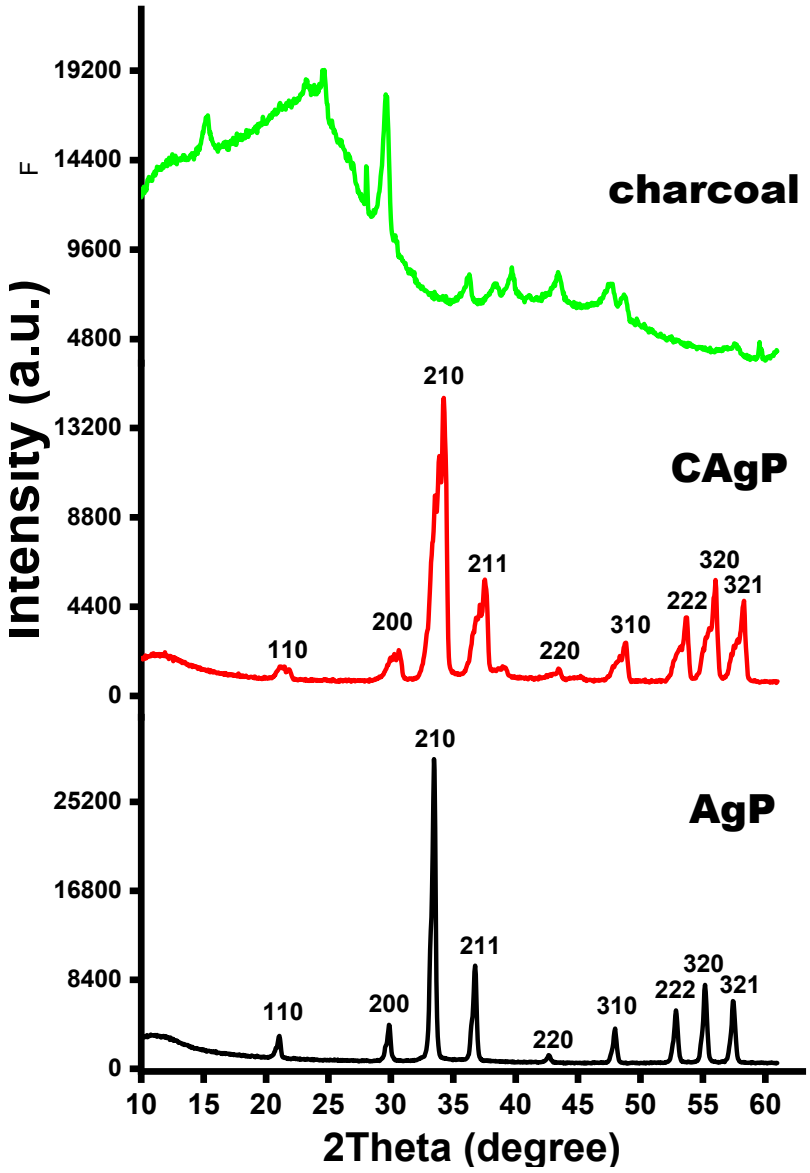

Figure 1: XRD patterns of charcoal, bare AgP and CAgP composites.

Fourier-transform infrared spectroscopy (FTIR) was used to validate the successful formation of the samples and also to confirm the presence of functional groups on their surfaces, Figure 2. The presence of vibrational peaks at 3000, 1654, and 1701 cm^{-1}, attributed to OH stretching, OH bending, and C=O stretching vibrations, respectively, confirm the presence of oxygen functionalities on the surface of treated charcoal, Figure 1a. In the FTIR spectrum of pure AgP,

Electronic copy available at: https://ssrn.com/abstract=4091672

characteristic peaks at 563, 1025 and 1412 cm^{-1} are respectively attributed to the bending vibration of O=P-O, and stretching vibrations of P=O (in PO^{3-}_4) and P–O–P (HPO^{2-}_4 ions) [21-23], suggesting successful AgP formation. The presence of adsorbed water molecules on the surface of AgP is confirmed by the stretching and bending vibrations of OH groups at 2771-3681 cm^{-1} and 1592 cm^{-1}, respectively, The bending and stretching vibration bands of the phosphate and OH groups in the FTIR spectrum of pure AgP are also present in the spectrum of CAgP, with the exception that due to the presence of charcoal, these peaks are slightly shifted to either lower or higher wavenumbers, confirming physical interaction between AgP and the treated charcoal to form CAgP. Similar observations have been reported when Ag_3PO_4 nanocrystals were immobilized on carbon nanostructures [21-23]. Due to the low content of charcoal used in the preparation of the composite, the vibrational bands of charcoal were masked by the strong and intense vibrational bands of AgP in the FTIR spectrum of CAgP.

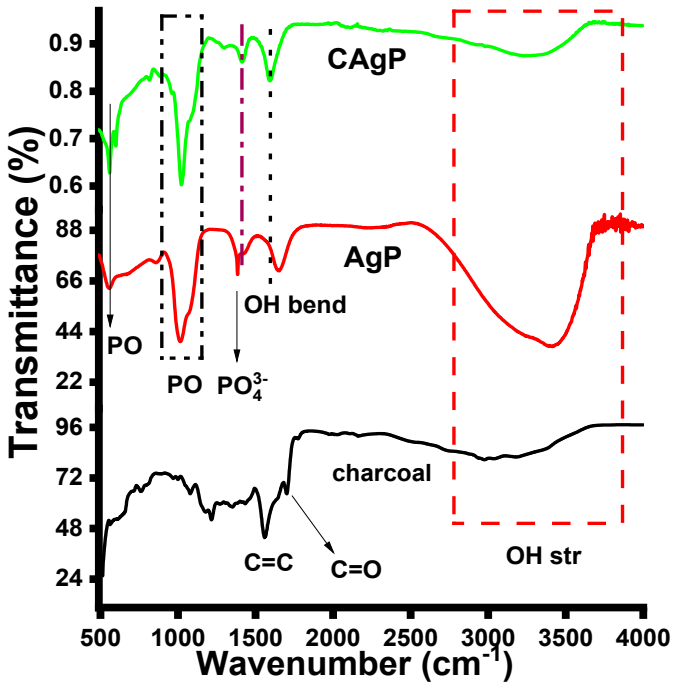

Figure 2. FTIR spectra of charcoal, bare AgP and CAgP composites.

Raman spectroscopy is a sensitive technique for determining the presence of functional groups and the degree of structural amorphization in carbon and carbon-based materials [24, 25]. The vibrational peaks at 589, 915, and 1009 cm^{-1} in the Raman spectrum of pure AgP correspond to the P–O–P symmetric stretching band, symmetric vibration, and asymmetric stretching vibration

Electronic copy available at: https://ssrn.com/abstract=4091672

of PO_4^{3-} ions, respectively, Figure 3 [26]. The D band at 1380 cm^{-1} and the G band at 1597 cm^{-1} in the Raman spectrum of treated charcoal are attributed to the chaos of crystalline structures and defection structures that are typical of carbonaceous materials [27, 28]. The presence of two prominent D and G vibrational bands associated with the charcoal at 1376 and 1605 cm^{-1}, respectively, as well as the intense symmetric vibrational band due to PO_4^{3-} ions at 912 cm^{-1}, substantially confirm the coexistence of AgP and charcoal in the CAgP composite. The ratio of intensity of D band to G band, (I_D/I_G), was used to determine the degree of structural amorphization of the charcoal before and after composition. The calculated I_D/I_G values of treated charcoal and CAgP are ≈ 0.86, indicating that in the presence of AgP, the graphitic crystallite layers of the charcoal remained relatively intact and undistorted. The I_D/I_G ratio of ~0.86 reported for charcoal and CAgP in this work are consistent with literature reports ranging from 0.86-1.20 [29]

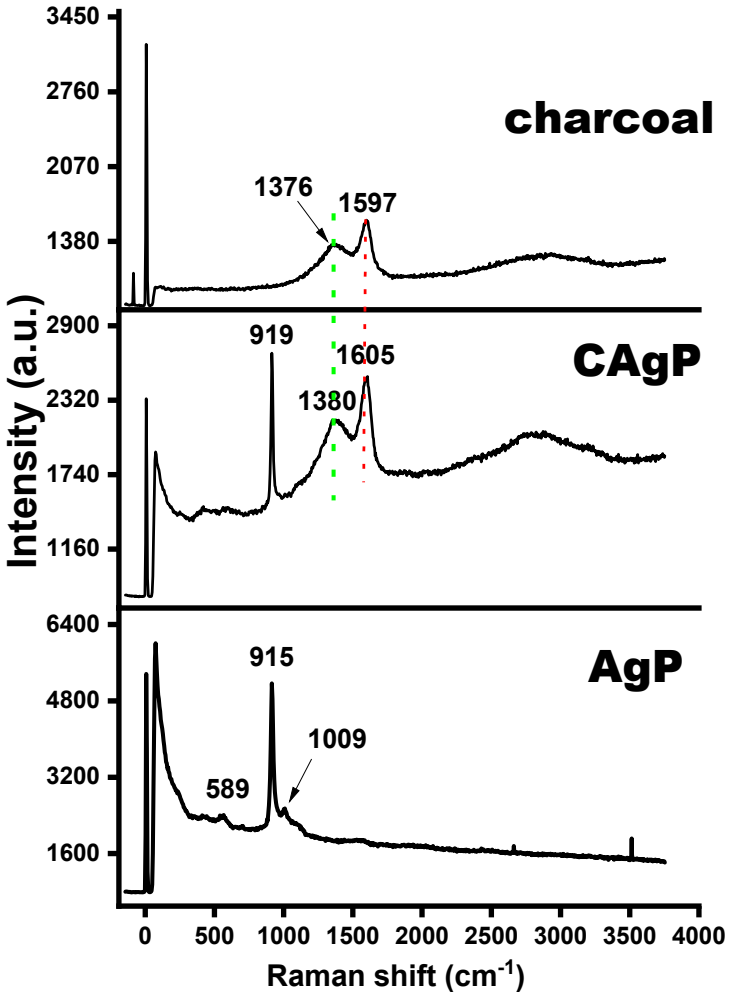

Electronic copy available at: https://ssrn.com/abstract=4091672

Figure 3: Raman spectra ofcharcoal, bare AgP and CAgP composite

The surface features of the prepared samples were revealed using a scanning electron microscope (SEM) in Figure 4. Figure 4a shows that the cascading layers (layers upon layers) of the graphitic structures of treated raw charcoal as viewed under SEM has rough surfaces and distorted shapes or sizes. The pristine AgP sample without charcoal had nanospherical morphologies with irregular sizes ranging from $0.4 - 0.5\mu m$, as revealed by the SEM image in Figure 4b. Because of the intra-particle interactions caused by their high surface energies in the nanoscale, the bare particles (of AgP NPs) appeared to aggregate and grow in size, Figure 4b. The AgP particles adhered to the surface of treated charcoal in the SEM image of CAgP composite, which is consistent with the graphitic layers of raw charcoal not being distorted during composition, Figure 4c. After being tethered to the surface of the charcoal to form CAgP, the shape of AgP particles remained fairly similar but the average sizes of the grains slightly reduced to $\approx 0.25 - 0.4\mu m$. Figure 4d shows that the major elemental compositions in CAgP composite are C, Ag, O, and P, and no other unwanted elements are detected, validating that CAgP was successfully formed and recovered in its pure form. The quantitative analysis from the EDX spectrum showed that the weigh% of C K, O K, P K, Ag L are 5.31, 18.85, 5.42 and 70.42%, respectively.

Electronic copy available at: https://ssrn.com/abstract=4091672

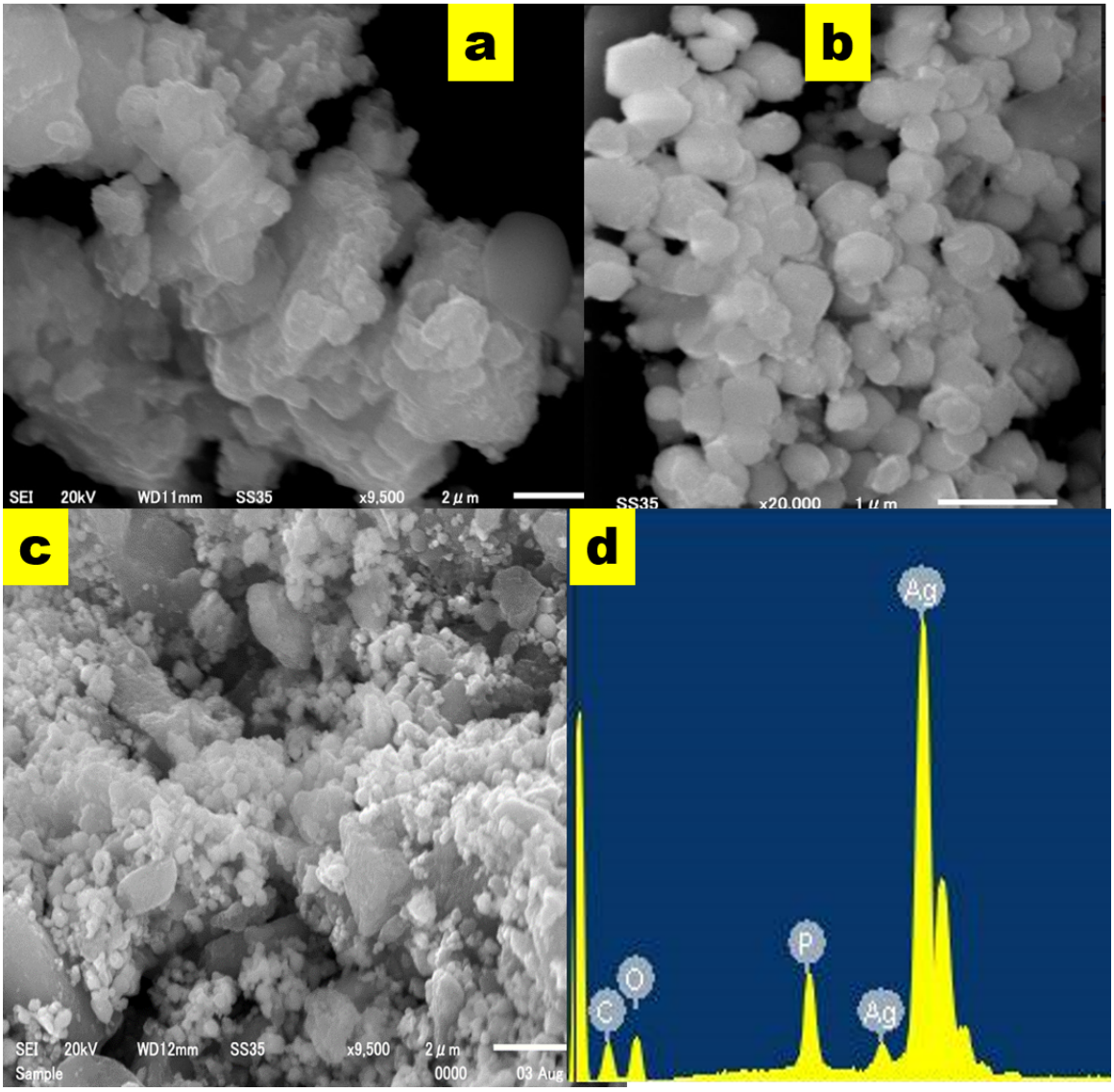

284

285 **Figure 4:** Scanning electron microscopeimages of (a) activated charcoal, (b) bare AgP (c)
286 activated charcoal passivated AgP (CAgP), and (d) Energy-dispersive X-ray spectroscope (EDX
287 or EDS) analysis of CAgP.

288 The transmission electron microscope (TEM) was also used to investigate the nanostructures and
289 morphologies of the prepared samples after sonication in abs. ethanol. TEM micrograph of treated
290 raw charcoal appeared as roughened layers of thin-sheets stacked on top of one another, Figure 5a.
291 Figure 5b shows that the uncoated particles of AgP clearly interacted with other neighbouring
292 particles in solution, resulting in highly aggregated particles [30]. By contrast, surface of the
293 charcoal became coarse after grains of AgP was tethered to it, indicating that the CAgP composite

Electronic copy available at: https://ssrn.com/abstract=4091672

was successfully formed, Figure 5c. The addition of charcoal as a solid substrate reduced the grain particle sizes of AgP, as well as reducing aggregation and improving the overall stability of the composite compared to pure AgP. The performance of the composite under light illumination will be improved due to the increased stability and reduced nanoparticle agglomeration.

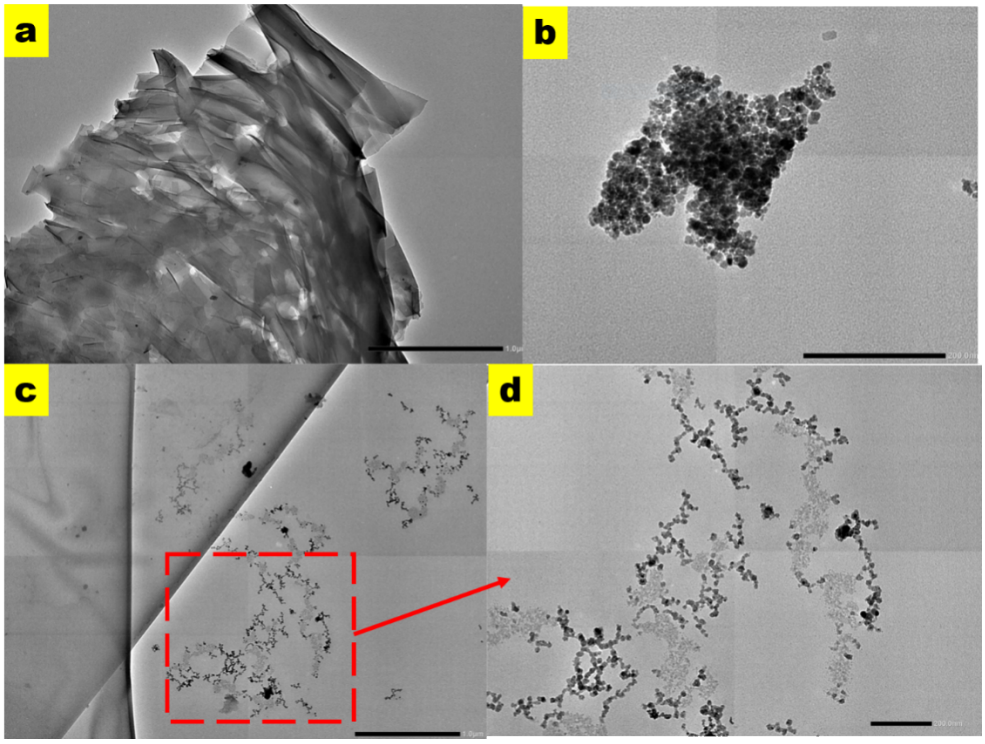

Figure 5: Transmission electron microscope (TEM) micrographs of (a) activated charcoal, (b) bare AgP, (c) CAgP and (d) enlarged image of CAgP under investigation from Figure 5c.

To elucidate the size distribution (hydrodynamic) of the synthesized samples, dynamic light scattering (DLS) measurements were performed at $50\ \mu g/mL$ for each sample in a mixture of methanol:water (1:10 v/v) [31]. According to the DLS data, raw charcoal has a size distribution ranging from $120 - 960$ nm. At a maximum intensity of ≈ 35 percent, the size distribution of pure AgP peaked at 530 nm, while the particle size of the CAgP composite shifted slightly to 459 nm, with maximum intensity peaking at 30%, Figure 6.

Electronic copy available at: https://ssrn.com/abstract=4091672

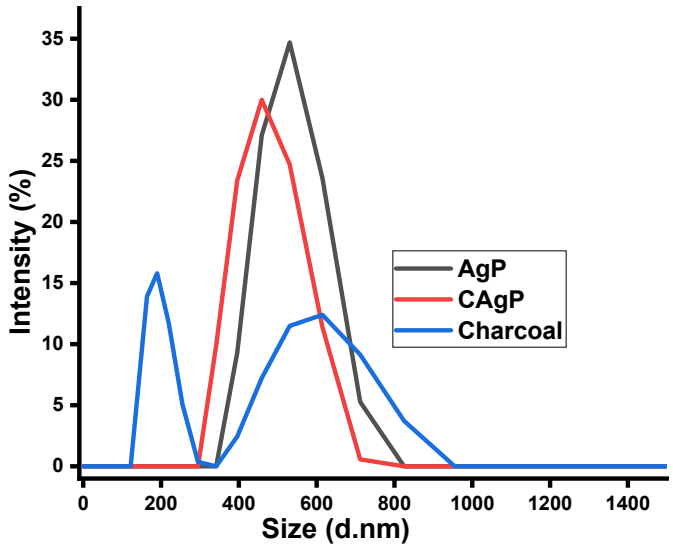

Figure 6: Dynamic light scattering (DLS) measurements of activated charcoal, bare AgP and CAgP composite.

The UV-Vis diffuse reflectance spectra of the photocatalysts (bare AgP and CAgP composite) and treated raw charcoal were used to investigate their energy band gap structures and light (UV or visible) absorption potentials, Figure 7. The UV absorption spectrum of treated charcoal shows intense absorption peak within the UV region at 260 nm which is due to the π–π* electronic transition of sp^2 graphitic carbon [32, 33], and no obvious absorption peak was observed in the visible region. Both AgP and CAgP show wide and strong absorption bands covering the entire UV and visible regions. In the UV-Vis absorption spectra of bare AgP and CAgP composite, the onset (wavelength) absorption band edges are 525 and 551 nm, respectively. The energy band gap of AgP at onset wavelength of 525 nm is 2.36 eV, while the energy band gap of CAgP extrapolated at absorption edge of 551 nm is 2.25 eV, Using **Eq. 2**.

$$E_g\,(eV) = 1240/\lambda \qquad \mathbf{2}$$

Where E_g is energy band gap (eV); and λ is onset (wavelength) absorption measured in nm.

Electronic copy available at: https://ssrn.com/abstract=4091672

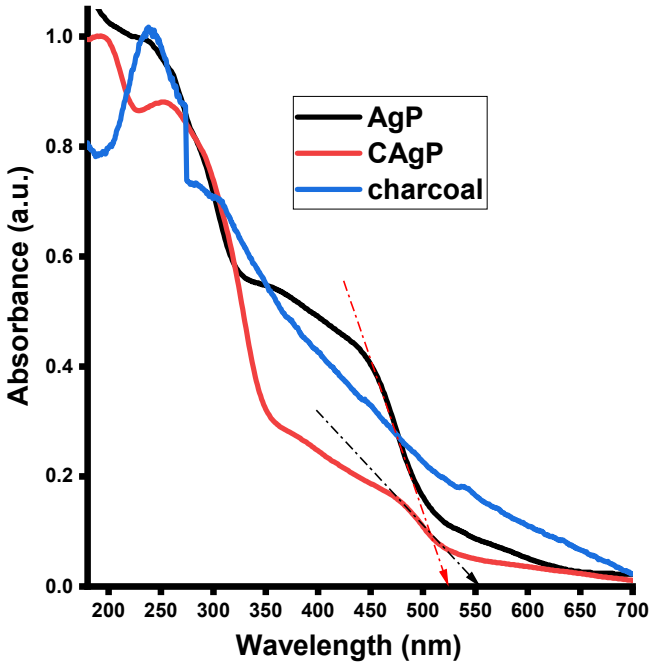

Figure 7: UV-Vis diffuse reflectance spectra of activated charcoal, bare AgP and CAgP composite.

The chemical constituents of CAgP composite and their atomic valence states was examined using X-ray photoelectron spectroscopy (XPS). From Figure 8, the overview of XPS analysis of CAgP composite shows that the wide survey has signals of P2p, C1s, Ag3d, O1s, Ag3p3, and Ag3p1 at binding energy of 133.4, 284.3, 367.1-373.4, 527, 573.4, and 604.1 eV, respectively. The signals and the respective binding energy positions are consistent and in good agreements with literature reports on XPS analysis of Ag_3PO_4, Figure 8 [34, 35]. The C1s signal in the XPS spectrum of CAgP was attributed to the raw charcoal used as a substrate for the immobilization of Ag_3PO_4, indicating that both charcoal and Ag_3PO_4 co-existed in the CAgP composite, Figure 9. The XPS spectrum of C1s signal was deconvoluted into three different peaks positioned at 284.5, 285.5, 287.1 eV, which are attributed to carbon atoms in sp^3 hybridized C-C, epoxy groups of C-O and carbonyl groups of C=O bonding states, respectively, Figure 9 [36,37]. The high resolution XPS spectrum of O 1s shows an intense peak and a smaller peak with binding energy peaks at 531.1 and 529.2 eV, respectively. The former peak at higher binding energy is associated with the oxygen in P–O–Ag bond, while the later peak at a lower binding energy was assigned to non-bridging oxygen atoms of P=O bond in Ag_3PO_4 [38]. The high resolution XPS spectrum of P 2p was resolved into a single binding energy peak at $\approx$ 133.5 eV, which corresponds to the +5 oxidation

Electronic copy available at: https://ssrn.com/abstract=4091672

state of phosphorus (P^{5+}) in PO_4^{3-} ion [39]. The core level Ag3d signal, which was resolved into two binding energy peaks at 367 eV and 373 eV are assigned to $3d_{5/2}$ and Ag $3d_{3/2}$, respectively. The two resolved binding energy peaks have spin-orbit separation of ≈ 6.0 eV, confirming that the valence state of Ag in CAgP is +1 [40].

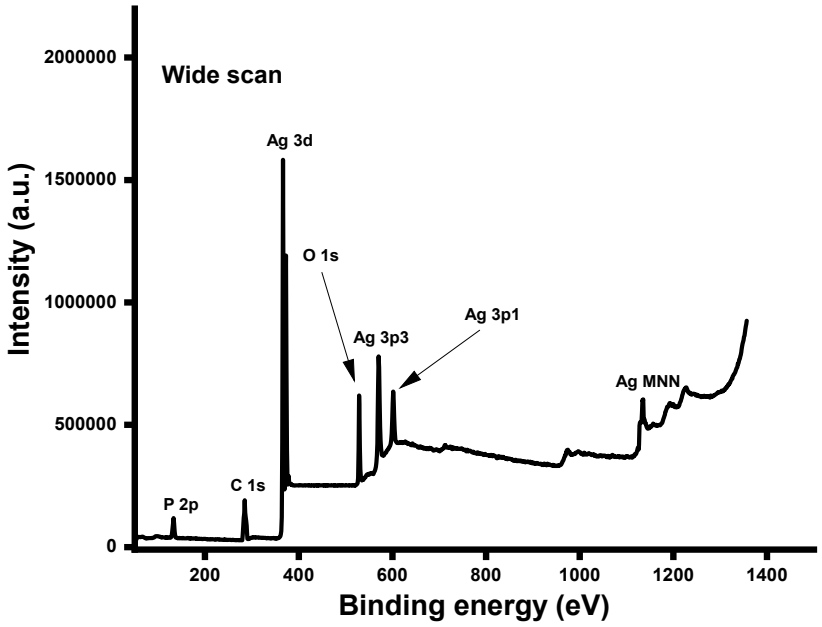

Figure 8: Representative XPS wide-scan survey spectrum taken from the surface of activated charcoal-AgP composite

Electronic copy available at: https://ssrn.com/abstract=4091672

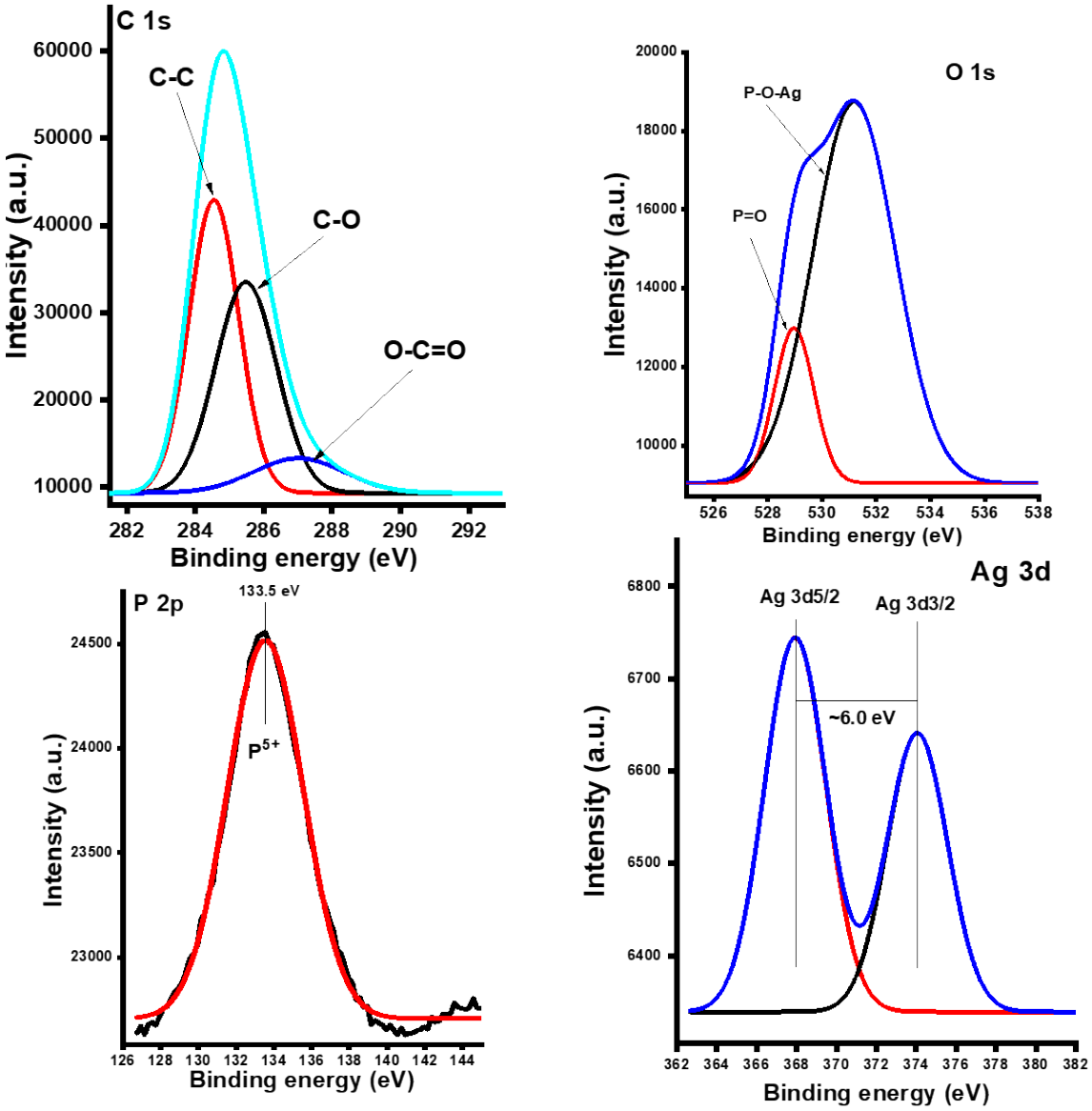

Figure 9: Deconvoluted XPS peaks of C 1s, O 1s, P 2p and Ag 3d for CAgP composite.

Photocatalytic generation of H_2O_2 over synthesized photocatalysts

The photocatalytic performances of AgP and CAgP were investigated for the formation of H_2O_2 in an O_2-saturated DI water under visible light illumination. Figure 10a shows the amount of H_2O_2 produced over AgP and CAgP composite as a function of time, ranging from 0-60 min in the dark to 1 to 6 h under visible light irradiations. To further rationalize the importance of the catalysts for the formation of peroxide, some control experiments were also carried out in the absence of the photocatalysts: by direct irradiation of the reaction mixture with 1 mM hole scavenger (FA) or

Electronic copy available at: https://ssrn.com/abstract=4091672

without addition of FA. The formation of peroxide was negligible under these control conditions, i.e., in the absence of photocatalysts, indicating that both FA and/or solar irradiation had no activity to produce hydrogen peroxide in the absence of catalysts, Figure 10a. Furthermore, catalytic control experiments conducted in the dark and in the presence of catalysts revealed negligible peroxide formation, which is an indication that the synthesized catalysts required the use of light illumination to generate charge carriers to produce peroxide in the solution. When O_2-saturated water was irradiated in the presence of AgP and CAgP catalysts, the yields of hydrogen peroxide increased nearly linearly over time up to 5 h, then plateaued at a constant level until 6 h. As a result, after 6 h of light irradiation, the formation of hydrogen peroxide over the catalysts peaked, indicating that a steady-state has been achieved in which the rate of H_2O_2 formation equals the rate of its decomposition, Figure 10a [41].The yields of peroxide when AgP and CAgP were added to O_2/H_2O/FA system were higher than the amounts of peroxide formed in O_2/H_2O system, Figure 10b. In Table 1, concentrations of AgP and CAgP in O_2/water solution without FA are 154 and 185μM, respectively. These values are significantly higher than the values reported for peroxide produced over bare CdS (27 μM) and CdS-G2 (128 μM) after 12 h of solar irradiation [15]. The results clearly show that in the absence of scavengers or special chemical compounds, significant amounts of hydrogen peroxide were produced over AgP and CAgP, demonstrating that both catalysts have the required thermodynamic feasibility to drive the formation of H_2O_2 and are thus suitable for the purpose of producing H_2O_2.In contrast, when O_2/water-containing FA solution was irradiated in the presence of AgP and CAgP, H_2O_2 concentrations of 222 and 371μM were formed, suggesting that the photocatalytic performances of catalysts/H_2O/FA system significantly differs from catalysts/H_2O system, with CAgP/H_2O/FA system showing the highest photocatalytic activity for H_2O_2 generation. This supports that the use of hole scavenger or electron donor is very crucial for generation of H_2O_2 via photocatalysis [2, 10].After 6 hours of light irradiation, the yields of peroxide produced in the CAgP/H_2O/FA system are up to 1.67, 2.00and2.06 times higher than the yields of peroxide produced in the AgP/H_2O/FA, AgP/H_2O and CAgP/H_2O systems, respectively, Table 1.

$$\mathrm{HCOOH} + h^+ \xrightarrow{CAgP/hv} \mathrm{CO_2} + 2\mathrm{H}^+ + e_{cb}^- \quad (3)$$

$$\mathrm{O_2} + e^- \xrightarrow{CAgP/hv} {}^{\bullet}\mathrm{O_2}^- \quad (4)$$

Electronic copy available at: https://ssrn.com/abstract=4091672

$$^{\bullet}O_2^- + H^+ \xrightarrow{CAgP/hv} {}^{\bullet}HO_2 \quad (5)$$

$$^{\bullet}HO_2 + e^- \xrightarrow{CAgP/hv} HO_2^- \quad (6)$$

$$HO_2^- + H^+ \xrightarrow{CAgP/hv} H_2O_2 \quad (7)$$

$$O_2 + 2H^+(HCOOH) + 2e^- \xrightarrow{CAgP/hv} H_2O_2 \quad (8)$$

$$O_2 + 2H^+(H_2O) + 2e^- \xrightarrow{CAgP/hv} H_2O_2 \quad (9)$$

The use of FA prevented the formation of holes in the VB of CAgP and simultaneously improved the ejection and transition of electrons from the VB to the CB of CAgP to facilitate the photocatalyzed H_2O_2 formation via two-electron reduction of dissolved molecular oxygen, **Eqns. 3-7** [2, 15, 42-44].In the first step, FA is decomposed by the visible light to form CO_2 and proton (H^+). The photo-excited electrons reacted with dissolved O_2 on the CAgP surface to form superoxide radicals ($^{\bullet}O_2^-$), **Eqn. 4**. The photogenerated protons (H^+) from FA decomposition reacted with O_2 to form hydroperoxyl radical ($^{\bullet}HO_2$), **Eqn. 5**, which was further reduced spontaneously by the electrons to form hydroperoxylanions (HO_2^-), **Eqn. 6**.In the final product, hydrogen peroxide was generated through reaction between hydroperoxyl anion and photogenerated proton H^+, **Eqn. 7**. Thus, the overall formation of H_2O_2 in CAgP/O_2/H_2O/FA which was attributed to the decomposition of FA in solution and reduction of O_2 by photoexcited electrons, is representedin **Eqn. 8**. In contrast, plausible mechanism for CAgP photocatalyzed H_2O_2 formation in the absence of FA (CAgP/O_2/H_2O), which was attributed to water oxidation and reduction of O_2 by electrons, is represented in **Eqn. 9**[15].Generally, the increased photocatalytic activity of CAgP over AgP can also be attributed to the strong interaction between AgP and the hydrophilic carbon used as a solid substrate. Even though the hydrophilic charcoal provides a good support for AgP (as in CAgP), it also serves as electron mediator by absorbing excess electrons from the conduction band via oxygen functionalities on its surface [12].In solution, bare AgP has an aggregation tendency, which reduces its light sensitivity, and resulting in less photocatalytic activity to generate H_2O_2*in situ*. Based on the high photocatalytic activity of

Electronic copy available at: https://ssrn.com/abstract=4091672

CAgP/FA system for H_2O_2 formation, further studies in terms of photocatalyst and hole scavenger dosages were conducted to optimize its catalytic activity.

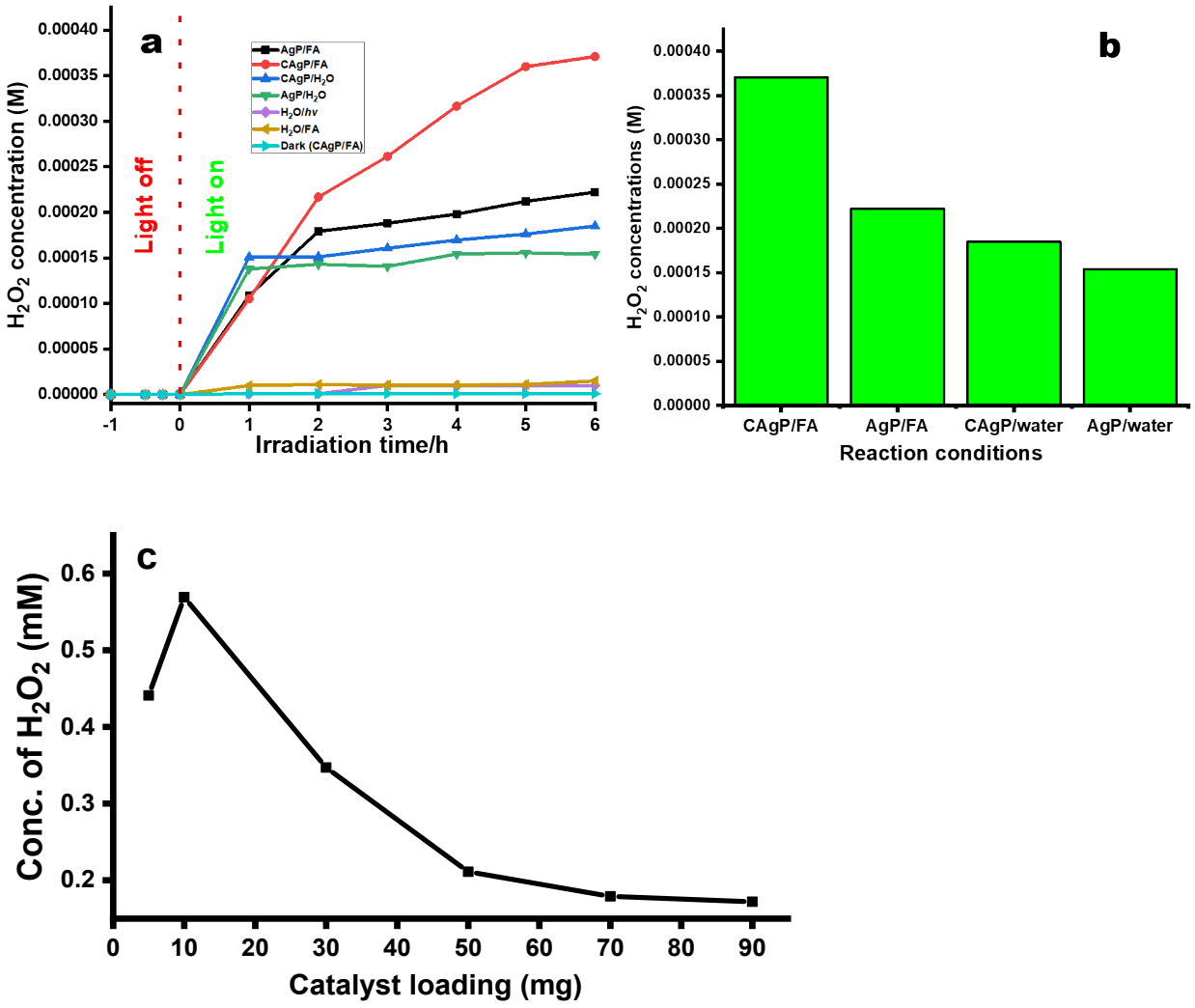

Figure 10: (a) Photocatalytic formation of H_2O_2 over bare AgP and CAgP under different experimental conditions, (b) formation of H_2O_2 over AgP and CAgP photocatalysts after 6 h light irradiation using either O_2/H_2O or O_2/H_2O/FA systems, and (c) formation of H_2O_2 over CAgP composite as a function of catalyst loading in O_2/H_2O/FA system.

Electronic copy available at: https://ssrn.com/abstract=4091672

Table 2: Concentration of H_2O_2 (in mM) over AgP and CAgP photocatalysts after 6 h light irradiation using either O_2/H_2O or O_2/H_2O/FA systems.

Time (h)	AgP/FA (mM)	CAgP/FA (mM)	AgP/H_2O (mM)	CAgP/H_2O (mM)
0	0	0	0	0
1	0.108	0. 105	0.151	0.138
2	0.179	0.217	0.151	0.143
3	0.188	0.261	0.161	0.141
4	0. 198	0.317	0. 170	0.154
5	0. 212	0.360	0.176	0.156
6	0.222	0.371	0.185	0.154

To determine the effect of catalyst dosage, the photocatalytic formation of H_2O_2 was demonstrated with various doses of CAgP in the presence of 0.5 mM formic acid (FA). Figure 11 depicts the catalyst-dependent profile of H_2O_2 formation under solar irradiation when CAgP dosage was varied from 5 to 90 mg. The catalytic efficiency of CAgP for H_2O_2 formation increased from 0.441 mM at 5mg and reach its optimal value at 0.569 mM with 10 mg catalyst dosage, implying that increasing catalyst dosage also leads to an increase in catalytic active and adsorption sites on CAgP, providing more sites for e^-/h^+ pair separation and facilitating transfer of photo-excited electrons from CB to oxygen molecules or protons to produce H_2O_2 [2]. As the catalyst dose was increased beyond the optimal 10 mg, the concentration of peroxide steadily decreased, reaching 0.179 mM at 70 mg, then remained fairly constant to 0.172 mM at 90 mg. The solution becomes increasingly turbid as the catalyst loadings in the reaction mixture increase, and more powders (CAgP) in solution coalesce into larger particles to induce aggregation, which reduces the amount of solar light penetrating into the reaction mixture, resulting in lower photocatalytic activity at higher catalytic doses.

Next we investigate the effect of formic acid (FA) on the catalytic formation of H_2O_2 in an O_2-saturated water system and in the presence of CAgP catalyst. Formic acid (FA) is an electron-

Electronic copy available at: https://ssrn.com/abstract=4091672

443 donating compound and also has high hydrogen content of about 4.4 wt.% which are often released
444 in solution upon its decomposition under solar irradiation [45]. The evolved hydrogen molecules
445 from HCOOH decomposition can react with *O2 to form H_2O_2,**Eqn. 8**, hence it is proposed here
446 as a source of H_2 to improve the overall formation of H_2O_2. The concentrations of FA were varied
447 from 0.5 to 2.5 mM and the solutions were irradiated with sunlight for 6 h. From Table 2 and
448 Figure 12, it was found that the amount of H_2O_2 formed increases steadily as the irradiation time
449 increases from 1 to 6 h for each FA concentration. However, after 6 h irradiation time, the amount
450 of H_2O_2 formed slightly decreased from 0.352 to 0.341 mM, corresponding to an increase in FA
451 concentration from 0.5 to 1.5 mM, followed by a sharp decline in the peroxide formation to 0.279
452 mM at 2.5 mM of FA. The results indicate that at FA concentrations below 1.5 mM, hydrogen
453 (H_2) produced (during FA decomposition) reacted with O_2 to produce a significant amount of
454 hydrogen peroxide, up to 0.352 mM, **Eqn. 8**. The excess FA in the solution at concentration above
455 1.5 mM may compete with the catalyst for visible light absorption, lowering light absorption
456 efficiency of CAgP, and reducing the rate of hydrogen evolution [46]. Thus, photocatalytic
457 formation of H_2O_2 is inhibited at higher FA concentrations [46]. It's worth noting that the
458 equivalent amount of H_2O_2 produced after 6 h of solar irradiation with 2.5 mM FA was achieved
459 in 3 h when 0.5 mM FA was used. As a result, FA concentration of 0.5 mM was selected as the
460 optimal value for hydrogen evolution, and to facilitate photo-induced hole trapping in order to
461 improve the photocatalytic performance of CAgP for hydrogen peroxide formation.

Electronic copy available at: https://ssrn.com/abstract=4091672

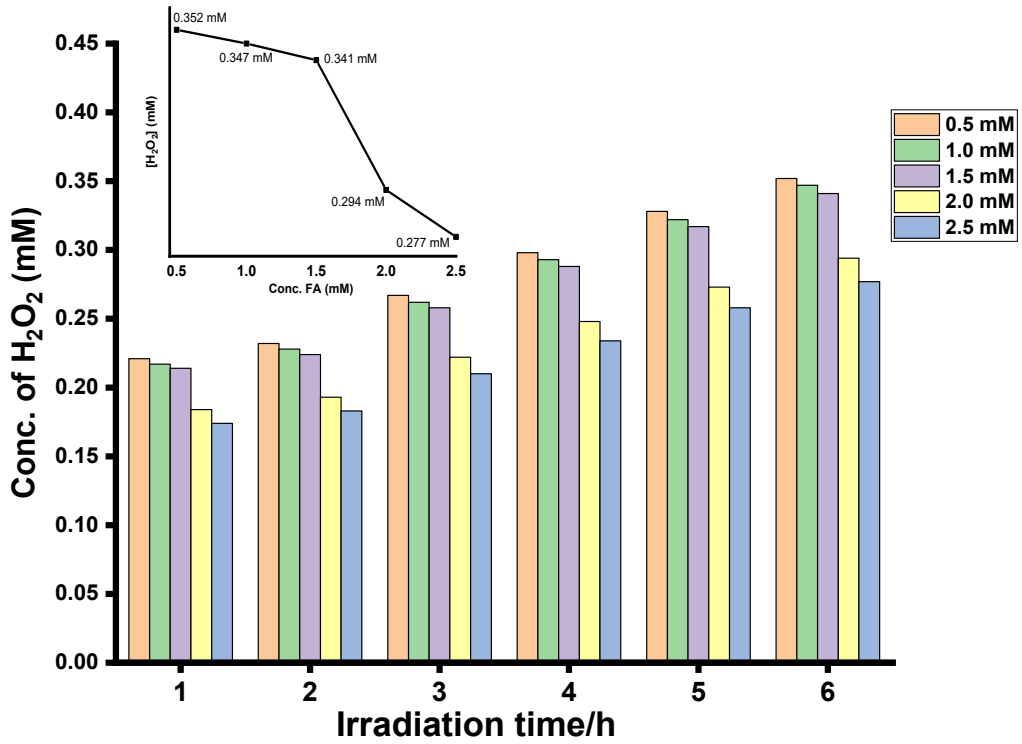

Figure 12: Photocatalytic formation of H_2O_2 over CAgP composite as a function of formic acid (FA) after 6 h of light irradiation in O_2/H_2O/FA system. [Conditions: catalyst dosage 30 mg, contact time 6 h, FA concentration: 0.5 to 2.5 mM, and temperature: 25 ± 2 °C].

Table 3: Amount of H_2O_2 produced over CAgP composite as a function of FA ranging from 0.5 to 2.5 mM for 6 h of light irradiation in O_2/H_2O/FA system.

Time (h)	0.5 (mM)	1.0 (mM)	1.5 (mM)	2.0 (mM)	2.5 (mM)
1	0.221	0.217	0.214	0.184	0.174
2	0.232	0.228	0.224	0.193	0.183
3	0.267	0.262	0.258	0.222	0.210
4	0.298	0.293	0.288	0.248	0.234
5	0.328	0.322	0.317	0.273	0.258
6	0.352	0.347	0.341	0.294	0.277

Electronic copy available at: https://ssrn.com/abstract=4091672

Trapping experiments and reaction mechanism

Having validated that CAgP or AgP catalysed formation of H_2O_2 are both possible in an air-saturated aqueous solution, we carried out further controlled trapping experiments to determine the effects of benzoquinone (BQ), $AgNO_3$, and isopropyl alcohol (*i*PA) which were used as superoxide, electron and hydroxyl radical scavengers, respectively, for the formation of H_2O_2. For the purpose of uniformity and clarity, previous experiments with CAgP/H_2O/FA were repeated and the results were compared to CAgP/H_2O/BQ,CAgP/H_2O/$AgNO_3$ and CAgP/H_2O/*i*PA systems. Figure 13 shows that the amount of H_2O_2 produced by CAgP/H_2O/$AgNO_3$ system was slightly higher than the amount reported for the CAgP/H_2O/FA system. The finding is intriguing and suggests that H_2O_2 can be formed not only by the e^- reduction of O_2 to form H_2O_2, but also by holes in the VB of the catalyst [47]. Thus, the formation of H_2O_2 in the absence of electrons can be hypothesized to occur via the oxidation of H_2O by holes to generate hydroxyl radicals ($^{\bullet}OH$), **Eqns. 10&11**, which is then followed by the combination of two $^{\bullet}HO$ to produce H_2O_2, **Eqn. 12**[10,47].When the $^{\bullet}O_2^-$ and $^{\bullet}HO$ radicals were trapped with 1 mM BQ and iPA, the amount of H_2O_2 formed in the solution was significantly suppressed and reduced to nearly 50% equivalent of the amount formed in the presence of FA and $AgNO_3$ at the same concentrations and volume. This suggests that the primary active species responsible for the generation of H_2O_2 are $^{\bullet}O_2^-$ and $^{\bullet}HO$, which were formed via electrons and holes in the CAgP catalyst, respectively.

$$H_2O \xrightarrow{h_{vb}^+} H^+ + OH^- \quad \textbf{10}$$

$$OH^- \xrightarrow{h_{vb}^+} + {}^{\bullet}OH \quad \textbf{11}$$

$$2{}^{\bullet}OH \rightarrow H_2O_2 \quad \textbf{12}$$

The mechanisms of the photocatalytic reactions is proposed and validated based on the positions of conduction band (CBE) and valence band edges (VBE) of CAgP under visible light irradiation. The potentials of CBE and VBE were determined using empirical Mulliken electronegativity equations, **Eqns. 13** and **14** [48]:

$$VBE = \chi - E^e + 0.5\,E_g \quad \textbf{13}$$

Electronic copy available at: https://ssrn.com/abstract=4091672

$$CBE = VBE - E_g \quad \textbf{14}$$

where χ, is the absolute electronegativity of semiconductor, Ag_3PO_4 (χ value of Ag_3PO_4is6.16 eV vs. NHE [49]),$E^e$is the energy of free electrons and about ~ 4.5 eV vs. NHE,$E_g$is the energy band gap of semiconductors (AgP = 2.36 eV and CAgP = 2.25 eV CAgP, as calculated from**Eqn. 2**). The VBE and CBE of AgP, and CAgP are 2.84/0.48 eV and 2.79/0.54 eV, respectively, Figure 14. For the photocatalytic reactions to be thermodynamically feasible, the redox potential of donors must be less positive than the potentials of VBE, and the redox potential of the acceptor must be less negative than the magnitude of potential edge of CB [50].Water oxidation by photo-induced holes is thermodynamically feasible, as the redox potential of $OH^-/^{\bullet}OH$ at $+1.99$ V vs. NHE is less positive than the potential of VBE of CAgP at $+2.79$ eV vs. NHE, Figure 15 [50]. Similarly, the photo-excited electrons could drive the reduction of O_2 to form H_2O_2 because the CBE of CAgP at ($+0.54$ eVvs. NHE) is more negative than the potential of O_2/H_2O_2 at 0.68 vs. NHE, Figure 15. As a result, the reactions in **Eqns. 8** and **12** are valid for the formation of H_2O_2.

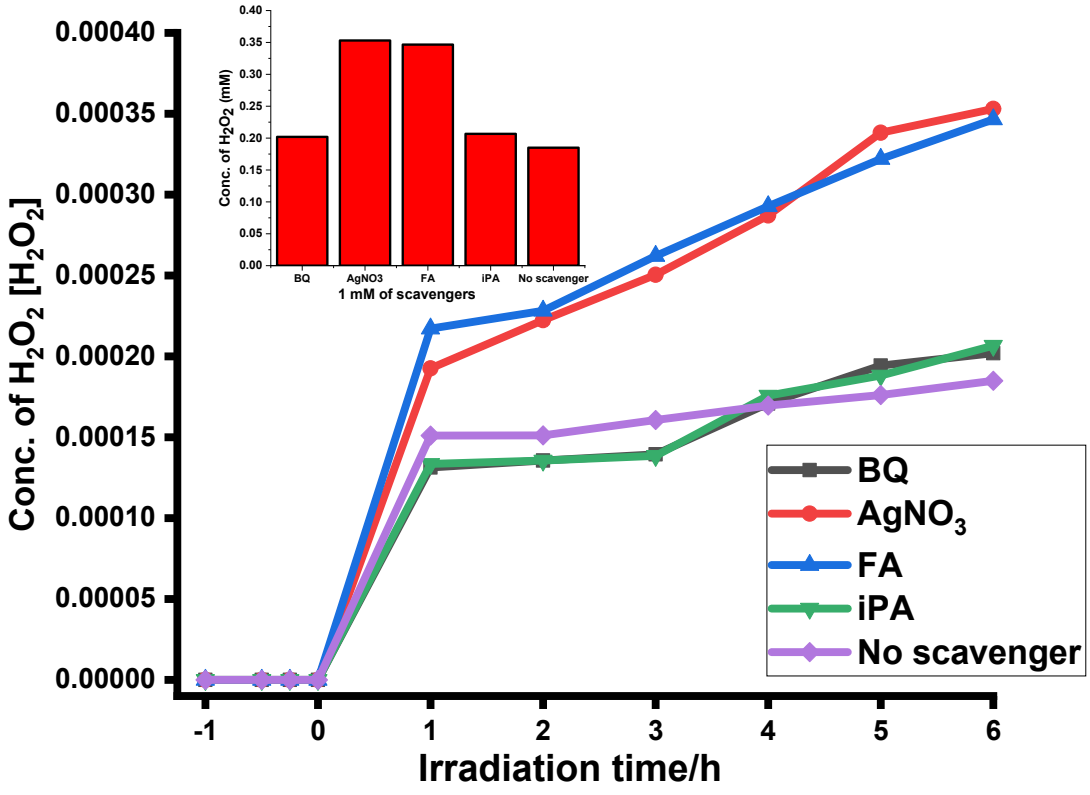

Electronic copy available at: https://ssrn.com/abstract=4091672

Figure 13: Effects of different scavengers on the photocatalytic formation of H_2O_2 over as-prepared CAgP composite. Inset: Amount of H_2O_2 produced over CAgP in the presence and absence of scavengers after 6 h of irradiation.

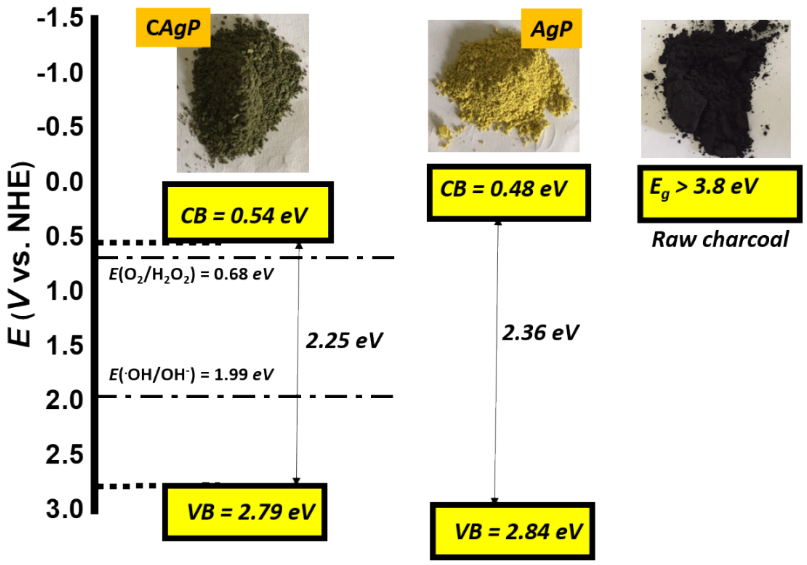

Figure 14: Energy band structures of charcoal, bare AgP, and CAgP composite.

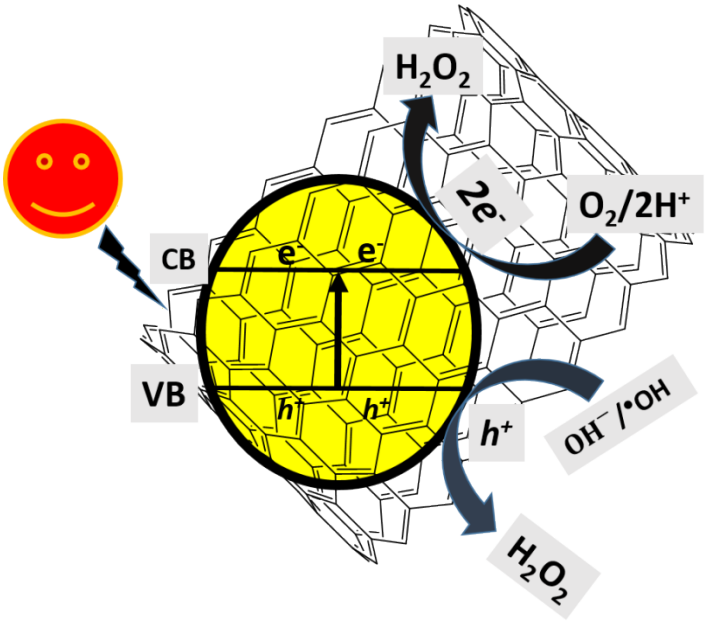

Figure 15: Schematic mechanism of H_2O_2 formation over as-synthesized CAgP (as representative) through photocatalytic reaction in aerated water.

Electronic copy available at: https://ssrn.com/abstract=4091672

Recovery and stability runs

Recovery, stability, and reusability are key features required in photoredox applications to ensure that the photocatalysts maintain their activities after prolonged exposure to light. Photostability performances of bare AgP and CAgP photocatalyzed H_2O_2 formation were evaluated by performing five recycle experiments under the same experimental conditions reported for O_2-saturated DI water, Figure 16. The photocatalytic performance of bare AgP was seen to gradually decrease in mass and activity from 100% to ~33% after the fifth recycle test, due to a number of factors, including uncontrollable aggregation of particles in solution, increased photo-corrosion and photo-decomposition of Ag_3PO_4 to Ag^o and $PO^{3}_{4}^{-}$, **Eqn. 15** [12]. Similar reports on the photo-excited electron induced deactivation/dissolution of silver-based photocatalysts have been reported in the literature [12].The stability of the CAgP composite, on the other hand, remained relatively stable until the fourth cycle test, when its catalytic activity dropped slightly below 90%, implying that the passivation of CAgP surface with activated charcoal reduced the rate of Ag_3PO_4 decomposition under solar illumination. Thus, CAgP has improved and remarkable photostability.

$$Ag_3PO_4 + 3e^- \rightarrow 3Ag^o + PO^{3}_{4}^{-} \quad \textbf{15}$$

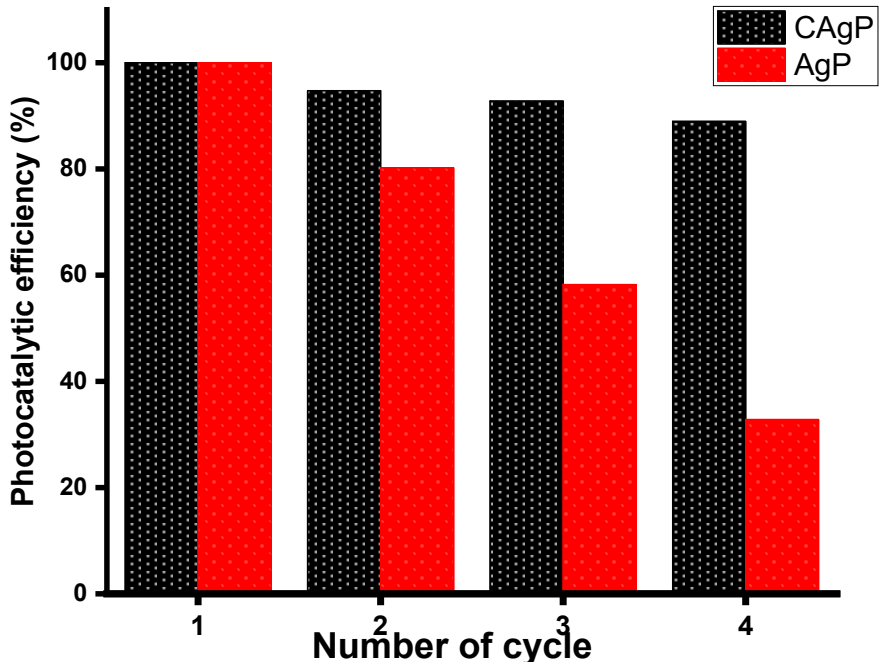

Electronic copy available at: https://ssrn.com/abstract=4091672

Figure 16: Plot of photocatalytic H_2O_2 formation efficiency (%) against number of cycles for photocatalytic stability evaluation of AgP and CAgP composite.

Conclusion

A cost-effective approach has been reported for the preparation of bare AgP and CAgP and their photocatalytic performances for hydrogen peroxide (H_2O_2) formation in O_2-saturated water was elucidated under natural solar illumination. The bare AgP was prepared by chemical precipitation method using disodium hydrogen phosphate (Na_2HPO_4) as a precipitating agent. CAgP was prepared in the same way as bare AgP, except that raw charcoal was first acidified in an aq. HCl solution and electrostatically interacted with Ag^+ before it was precipitated as Ag_3PO_4 on the surface of activated charcoal using Na_2HPO_4.The as-synthesized bare AgP and CAgP cmposite were characterized using techniques such as XRD, FT-IR, Raman, TEM, SEM, EDX, and XPS. The CAgP composite demonstrated remarkable photocatalyzed H_2O_2 production compared to bare AgP nanoparticles, due to the presence of activated charcoal, which serves as a solid support for Ag_3PO_4 and reduces the chance of photodecomposition of Ag_3PO_4under solar irradiation. Additionally, the activated carbon improved electron mobility and charge carrier separation via oxygen groups on its surface.In the presence of FA (O_2/H_2O/FA system) as a hole scavenger, H_2O_2 formation over CAgP was thermodynamically facilitated by $2e^-$ reduction of dissolved molecular oxygen; while the second pathway involved water oxidation by photo-induced holes and combination of the two photogenerated $^{\bullet}HO$ to formH_2O_2in the presence of $AgNO_3$(O_2/H_2O/ $AgNO_3$ system) as an electron scavenger. Thus, through $2e^-$ reduction of dissolved O_2 and water oxidation, CAgP satisfy two-channel pathways for H_2O_2 formation.

Author contributions

Conceptualization, resources; review and editing: Owolabi M. Bankole, Adeniyi S. Ogunlaja, Ojodomo A. Achadu, and Segun E. Olaseni.

Data curation, formal analysis, methodology: Kehinde I. Ojubola, Olayinka S. Adanlawo, Faith O. Adeyemi, Joseph B. Ogunniyi and Segun E. Olaseni.

Original draft writing: Owolabi M. Bankole

Supervision; validation, visualization: Owolabi M. Bankole, and Segun E. Olaseni.

Electronic copy available at: https://ssrn.com/abstract=4091672

REFERENCES

1. S. Siahrostami, S. J. Villegas, A. H. B. Mostaghimi, S. Back, A. B. Farimani, H. Wang, K. A. Persson, J. H. Montoya, Review on Challenges and Successes in Atomic-Scale Design of Catalysts for Electrochemical Synthesis of Hydrogen Peroxide, ACS Catal. 2020, 10, 14, 7495–7511A.
2. H. Hou, X. Zeng, X. Zhang, Production of Hydrogen Peroxide by Photocatalytic Processes, Angewandte Chemie 59 (40) (2020) 17356-17376.
3. S.A.M. Shaegh, N.T. Nguyen, S.M.M. Ehteshami, S.H. Chan, Energy Environ. Sci. 5 (2012) 8225–8228.
4. J. M. Campos-Martin, G. Blanco-Brieva, J. L. Fierro, Angew. Chem., Int. Ed. 2006, 45, 6962-6984.
5. R. Guan, X. Yuan, Z. Wu, L. Jiang, Y, Li, G. Zeng, Principle and application of hydrogen peroxide based advanced oxidation processes in activated sludge treatment: A reviewChemical Engineering Journal 339 (2018) 519-530.
6. S. Yamazaki, Z. Siroma, H. Senoh, T. Ioroi, N. Fujiwara and K. Yasuda, J. Power Sources, 2008, 178, 20–25.
7. X. Jia, F. Sun, Y. Fei, M. Jin, F. Zhang, W. Xu, N. Shi, Z. Lv, Explosion characteristics of mixtures containing hydrogen peroxide and working solution in the anthraquinone route to hydrogen peroxide, Process Safety and Environmental Protection 119 (2018) 218–222.
8. M. Kurian, Advanced oxidation processes and nanomaterials-a review, Cleaner Engineering and Technology 2 (2021) 100090.
9. D. Tsukamoto, A. Shiro, Y. Shiraishi, Y. Sugano, S. Ichikawa, S. Tanaka, T. Hirai, Photocatalytic H2O2 production from ethanol/O2 System using TiO2Loaded with Au–Ag bimetallic alloy nanoparticles, ACS Catal. 2 (4) (2012) 599–603.
10. Y. Wang, S. Hu, Q. Li, G. Gu, Y. Zhao, H. Liang, W. Li, One step synthesis of high-efficiency AgBr–Br–gC3N4 composite catalysts for photocatalytic H2O2 production via two channel pathway, RSC Adv., 2018, 8, 36903–36909.

Electronic copy available at: https://ssrn.com/abstract=4091672

11. S. Pal, S. Kumar, A. Verma, A. Kumar, T. Ludwig, M. Frank, S. Mathur, R. Prakash, I. Sinha, Development of magnetically recyclable visible light photocatalysts for hydrogen peroxide production, Materials Science in Semiconductor Processing 112 (2020) 105024.
12. B. Weng, M.-Y. Qi, C. Han, Z.-R. Tang, Y.-J. Xu, Photocorrosion inhibition of semiconductor-based photocatalysts: Basic principle, current development, and future perspective, ACS Catal. 9 (2019) 4642−4687.
13. O. M. Bankole, K. I. Ojubola, O.S. Adanlawo, K.A. Oluwafemi, A.O. Adedapo, M.A. Adeyemo, S.E. Olaseni, N.A. Oladoja, E.J. Olivier, E.E. Ferg, A.S. Ogunlaja, Atmospheric CO2 mediated formation of Ag2O-Ag2CO3/g-C3N4 (p-n/n-n dual heterojunctions) with enhanced photoreduction of hexavalent chromium and nitrophenols, Journal of Photochemistry and Photobiology A: Chemistry 427 (2022) 113800.
14. X. Yang, H. Cui, Y. Li, J. Qin, R. Zhang, H. Tang ACS Catal., 3 (3) (2013) 363-369.
15. S. Thakur, T. Kshetri, N. H. Kim, J. H. Lee, Sunlight-driven sustainable production of hydrogen peroxide using aCdS–graphene hybrid photocatalyst, Journal of Catalysis 345 (2017) 78–86.
16. J. K. Lee, K. L. Walker, H. S. Han, J. Kang, F. B. Prinz, R. M. Waymouth, H. G. Nam, R. N. Zare, Spontaneous generation of hydrogen peroxide from aqueous microdroplets, PNAS 116 (39) (2019) 19294–19298.
17. R. M. Sellers, Spectrophotometric determination of hydrogen peroxide using potassium titanium (IV) oxalate, Analyst 105 (1990) 950-954.
18. R. Dhawle, Z. Frontistis, D. Mantzavinos, P, Lianos, Production of hydrogen peroxide with a photocatalytic fuel cell and its application to UV/H2O2 degradation of dyes, Chem. Eng. J. Adv. 6 (2021) 100109.
19. G. Xiao, R. Xiao, B. Jin, W. Zuo, J. Liu, J. R. Grace, Study on Electrical Resistivity of Rice Straw Charcoal, Journal of Biobased Materials and Bioenergy, 4, 426–429, 2010.
20. T. Wang, Y. Wang, Y. Wu, L. Zhou, Y. Jin, W. Liu, J. Huang, X. Fang, X. Tang, LiFePO4/C Composite Prepared by Coal Based Carbon Sources, Int. J. Electrochem. Sci., 12 (2017) 975 – 984.
21. K.H. Kim, J.M. Jeong, S.J. Lee, B.G. Choi, K.G. Lee, Protein-directed assembly of cobalt phosphate hybrid nanoflowers. J. Colloid Interface Sci. 2016, 484, 44–50.

Electronic copy available at: https://ssrn.com/abstract=4091672

22. L. Zhou, O.G. Alvarez, C.S. Mazon, L. Chen, H. Deng, M. Sui, The roles of conjugations of graphene and Ag in Ag_3PO_4-based photocatalysts for degradation of sulfamethoxazole. Cataly Sci Technol 6 (2016)5972–5981.
23. N. Nourieh, R. Nabizadeh, M. A. Faramarzi, S. Nasseri, K. Yaghmaeian, B. Mahmoudi, M. Alimohammadi, M. Khoobi, Photocatalytic degradation of ketoconazole by Z-scheme Ag3PO4/graphene oxide: response surface modeling and optimization, Environ Sci Pollut Res. 27, pages250–263 (2020).
24. A. Sadezky, H. Muckenhuber, H. Grothe, R. Niessner, U. Pöschl, Carbon 2005, 43, 1731–1742.
25. X. Xu, W. Song, D.G. Huang, B.Y. Gao, Y.Y. Sun, Q.Y. Yue, K.F. Fu, Colloids Surf. A Physicochem. Eng. Asp. 2015, 476, 68–75.
26. A. Reheman, Y. Tursun, T. Dilinuer, M. Halidan, K. Kadeer, A. Abulizi, Nanoscale Res. Lett. 13, 70 (2018).
27. R.J. Nemanich, S.A. Solin, Phys. Rev. B. 1979, 20, 392–401.
28. X.X. Zhou, X. Qu, R. Zhang, J.C. Bi, Fuel Process. Technol. 2015, 135, 195–202.
29. N. Zhao, J. Wang, C. Shi, E. Liu, J. Li, C. He, Chemical vapor deposition synthesis of carbon nanospheres over Fe-based glassy alloy particles, J. Alloy Compd. (2014) 816-822.
30. H.H. Liu, S. Surawanvijit, R. Rallo, G. Orkoulas, Y. Cohen, Analysis of nanoparticle agglomeration in aqueous suspensions via constant-number Monte Carlo simulation, Environ. Sci. Technol. 45 (2011) 9284–9292.
31. S. Bhattacharjee, DLS and zeta potential – What they are and what they are not? Journal of Controlled Release 235 (2016) 337–351.
32. M. Sharif Sh, F. Golestani Fard, E. Khatibi, H. Sarpoolaky, Dispersion and stability of carbon black nanoparticles, studied by ultraviolet–visible spectroscopy, J. Taiwan Instit. Chem. Eng. 40 (5) (2009) 524–527.
33. L. Jena, D. Soren, P. K. Deheri, P. Pattojoshi, Preparation, characterization and optical properties evaluations of bamboo charcoal, Current Research in Green and Sustainable Chemistry 4 (2021) 100077.
34. Q. S. Yan, M. M. Xu, C. P. Lin, J. F. Hu, Y. G. Liu, R. Q. Zhang, Efficient photocatalytic degradation of tetracycline hydrochloride by Ag3PO4 under visible-light irradiation, Environ Sci Pollut Res. Int. 2016 23(14):14422-14430.

Electronic copy available at: https://ssrn.com/abstract=4091672

35. W. Zhang, L. Zhou, J. Shi, H. Deng, Synthesis of Ag3PO4/G-C3N4 composite with enhanced photocatalytic performance for the photodegradation of diclofenac under visible light irradiation, Catalysts (2018) 8, 45-60.
36. M. I. Shinger, A. M. Idris, D. D. Qin, H. Baballa, D. Shan, X. Lu, Simulated sunlight induced the degradation of rhodamine B over graphene oxide-based Ag3PO4@AgCl, Int. J. Mater. Sci. Appl. 2015; 4(4): 246-255.
37. L. Zhang, L. Tu, Y. Liang, Q. Chen, Z. Li, C. Li, Z. Wanga, W. Li, Coconut-based activated carbon fibers for efficient adsorption of various organic dyes, RSC Adv., 2018, 8, 42280–42291.
38. P. Dong, G. Hou, C. Liu, X. Zhang, H. Tian, F. Xu, X. Xi, R. Shao, Origin of Activity and Stability Enhancement for Ag3PO4 Photocatalyst after Calcination, Materials, 2016, 9, 1–17.
39. M. Ge, N. Zhu, Y.P. Zhao, J. Li, L. Liu, Sunlight-assisted degradation of dye Pollutants in Ag3PO4 suspension, Ind. Eng. Chem. Res, 2012, 51, 5167-5173.
40. Y. Bu, Z. Chen, Role of polyaniline on the photocatalytic degradation and stability performance of the polyaniline/silver/silver phosphate composite under visible light, ACS Appl. Mater. Interfaces, 2014, 6, 17589–17598.
41. M. Teranishi, S. Naya, H. Tada, In situ liquid phase synthesis of hydrogen peroxide from molecular oxygen using gold nanoparticle-loaded titanium (IV) dioxide photocatalyst, J. Am. Chem. Soc., 2010, 132, 7850–7851.
42. Y. Ji, Y. Luo, Structure-dependent photocatalytic decomposition of formic acid on the anatase TiO_2 (101) surface and strategies to increase its reaction rate. J. Power Sources 306 (2016) 208–212.
43. S. Civiš, M. Ferus, M. Zukalová, P. Kubát, L. Kavan, Photochemistry and gas-phase FTIR spectroscopy of formic acid interaction with anatase $Ti^{18}O_2$ nanoparticles. J. Phys. Chem. C 116 (2012) 11200–11205.
44. M. Navlani-García, D. Salinas-Torres, K. Moria, Y. Kuwahara, H. Yamashita, Photocatalytic approaches for the hydrogen production via formic acid decomposition, Topics in Current Chemistry, Top Curr Chem (Z) 377 (2019) 27.
45. V. V. Chesnokov, P. P. Dik, A. S. Chichkan, Formic acid as a hydrogen donor for catalytic transformations of tar, Energies 13(17) (2020) 4515.

Electronic copy available at: https://ssrn.com/abstract=4091672

685 46. W. Wang, B. Li, H.-J. Yang, Y. Liu, L. Gurusamy, L. Karuppasamy, J. J. Wu,
686 Photocatalytic hydrogen evolution from water splitting using core-shell structured
687 Cu/ZnS/COF composites, Nanomaterials 11 (2021) 3380.
688 47. L. P. Yang, G. H. Dong, D. L. Jacobs, Y. H. Wang, L. Zang, C. Y. Wang, Two-channel
689 photocatalytic production of H2O2 over g-C3N4 nanosheets modified with perylene
690 imides, J. Catal., 2017, 352, 274–281.
691 48. J. Jiang, X. Zhang, P. Sun, L. Zhang, ZnO/BiOI Heterostructures: Photoinduced charge-
692 transfer property and enhanced visible-light photocatalytic activity, J. Phys. Chem. C, 115
693 (2011) 20555-20564.
694 49. Z. Chen, W. Wang, Z. Zhang, X. Fang, High-efficiency visible-light-driven Ag3PO4/AgI
695 photocatalysts: Z-scheme photocatalytic mechanism for their enhanced photocatalytic
696 activity. J Phys Chem C 117 (2013) 19346–19352.
697 50. T. Liu, L. Wang, X. Lu, J. Fan, X. Cai, B. Gao, R. Miao, J. Wang, Y. Lv, Comparative
698 study of the photocatalytic performance for the degradation of different dyes by ZnIn2S4:
699 adsorption, active species, and pathways, RSC Adv. 7 (2017) 12292–12300.

700

Electronic copy available at: https://ssrn.com/abstract=4091672